Anatomical Based FDG-PET Reconstruction for the Detection of Hypo-metabolic Regions in Epilepsy

Kristof Baete, *Student Member, IEEE,* Johan Nuyts, *Member, IEEE,* Wim Van Paesschen, Paul Suetens, *Member, IEEE,* and Patrick Dupont

***Abstract*— Positron emission tomography (PET) of the cerebral glucose metabolism has shown to be useful in the presurgical evaluation of patients with epilepsy. Between seizures, PET images using fluorodeoxyglucose (FDG) show a decreased glucose metabolism in areas of the gray matter (GM) tissue that are associated with the epileptogenic region. However, detection of subtle hypo-metabolic regions is limited by noise in the projection data and the relatively small thickness of the GM tissue compared to the spatial resolution of the PET system. Therefore, we present an iterative maximum-a-posteriori based reconstruction algorithm, dedicated to the detection of hypo-metabolic regions in FDG-PET images of the brain of epilepsy patients. Anatomical information, derived from magnetic resonance imaging data, and pathophysiological knowledge was included in the reconstruction algorithm. Two Monte-Carlo based brain software phantom experiments were used to examine the performance of the algorithm. In the first experiment, we used perfect, and in the second, imperfect anatomical knowledge during the reconstruction process. In both experiments, we measured signal-to-noise ratio (SNR), root mean squared bias (rms) and rms standard deviation. For both experiments, bias was reduced at matched noise levels, when compared to post-smoothed maximum-likelihood (ML-EM) and maximum-a-posteriori reconstruction without anatomical priors. The SNR was similar to that of ML-EM with optimal post-smoothing, although the parameters of the prior distributions were not optimized. We can conclude that the use of anatomical information combined with prior information about the underlying pathology is very promising for the detection of subtle hypo-metabolic regions in the brain of patients with epilepsy.**

***Index Terms*— Image processing, magnetic resonance imaging, MAP estimation, positron emission tomography**

I. Introduction

EPILEPTIC seizures are known to be the result of abnormal discharges of a group of nerve cells in specific areas in the gray matter (GM) tissue of the brain [1]. Surgical removal of the epileptogenic region in the brain can cure patients with refractory partial epilepsy. Positron emission tomography (PET) of the cerebral glucose metabolism between seizures, using 2-[^{18}F]fluoro-2-deoxy-D-glucose (FDG), has shown to be useful in the presurgical evaluation process [2], [3]. In fact, PET can replace more invasive diagnostic procedures, such as e.g. the surgical insertion of depth electrodes into deep brain structures [4]. These invasive methods are associated with substantial risk to the patient compared to a non-invasive PET scan.

Between seizures, FDG-PET images of the brain of patients with refractory partial epilepsy often show a decreased glucose metabolism in certain areas of the GM. Usually, these hypo-metabolic regions are associated with the epileptogenic region, i.e. the region that includes the lesion which causes the epileptic seizures. Unfortunately, detection problems arise when these regions are more subtle. Moreover, the image quality can have a serious influence on the detection task.

The image quality of PET is severely affected by noise in the measurement. This is caused by a variety of physical effects, like e.g. the physical decay of the limited amount of radio-pharmaceutical that can be administered to the patient and the limited scanning duration that is achievable in a clinical environment. Furthermore, structures having small spatial dimensions are very hard to resolve using emission tomography because of the limited spatial resolution of the system. This is an important issue when imaging the human brain, since this organ exhibits a rather complex anatomical structure and the GM thickness can be relatively small (about 3 mm, [5]). Furthermore, there can be a large variation in thickness and geometry of several of the brain substructures. This might cause an underestimation of the tracer activity in the reconstructed image [6]. This effect, called the partial volume effect, can lead to spurious hypo-metabolic regions. In the presurgical evaluation, this can result in an increased amount of false positive predicted hypo-metabolic regions. Moreover, if the finite spatial resolution of the imaging system is not accounted for, a possible spill over of activity to neighboring regions can occur in the reconstructed PET image. This can yield a possible misinterpretation of the extent of hypo-metabolic regions. Thereby, presurgical delineation of these regions becomes more difficult and less accurate.

Over the years, many groups developed reconstruction algorithms and designed techniques to handle these problems. Recently, some groups explored techniques for the use of anatomical information. As part of the basic epilepsy presurgical evaluation protocol, high-resolution magnetic resonance (MR) images are acquired. Since this information is always available, it can be used as additional information in emission tomography. In general, literature shows two methodological categories: (a) use of anatomical information after the reconstruction process and (b) including the anatomical information in an iterative reconstruction technique. The work presented

This work was supported by K.U.Leuven grants IDO-99/005, OT-00/32 and F.W.O. grant G.0174.03.

K. Baete, J. Nuyts and P. Dupont are with the Department of Nuclear Medicine, UZ Gasthuisberg, Katholieke Universiteit Leuven, B-3000 Leuven, Belgium (e-mail: kristof.baete@uz.kuleuven.ac.be).

W. Van Paesschen is with the Department of Neurology, UZ Gasthuisberg, Katholieke Universiteit Leuven, B-3000 Leuven, Belgium.

P. Suetens is with the Laboratory for Medical Image Computing, Radiology-ESAT/PSI, UZ Gasthuisberg, Katholieke Universiteit Leuven, B-3000 Leuven, Belgium.

in this paper is based on the latter approach, however the approximation of a tissue composition model, used in post-processing methods, is used here as well. The post-processing method, we refer to, is dedicated for partial volume correction in the GM tissue [7]. The iterative reconstruction framework, that will be used here, exhibits more flexibility for modeling different kinds of physical effects, including the incorporation of anatomical information. For example, this can be anatomical based weighting of Gibbs smoothing priors [8]–[10], imposing a Gaussian distribution for the activity within a tissue region [10], [11], minimum cross-entropy reconstruction techniques using anatomical based edge preserved smoothing [12], or using a joint mixture framework [13]. We refer to these papers for an overview of other approaches.

Specific for epilepsy, there is even more a priori information at our disposal, i.e. knowledge about the pathophysiology of the glucose metabolism in epilepsy. Therefore, in the next sections of this paper, we will present the derivation of an iterative reconstruction algorithm for PET projection data of the cerebral glucose metabolism using FDG. This algorithm is dedicated for the detection of hypo-metabolic regions in the GM, using anatomical information and knowledge about the pathophysiology of the glucose metabolism in epilepsy.

II. Methodology

In a first step, we give an explicit formulation of the a priori knowledge used in the reconstruction algorithm. Thereafter, the algorithm itself is presented.

A. Assumptions

The metabolic activity of the white matter (WM) is much lower and much more uniform than in gray matter [14], [15]. Moreover, no tracer accumulation is expected in the cerebrospinal fluid (CSF) during the measurement. The identification of GM, WM and CSF is obtained from a high-resolution anatomical MR image of the brain. We assume that this MRI is normal. Current brain segmentation algorithms [16] can very accurately determine these three tissue classes. The remaining unlabeled voxels are grouped in an additional class, labeled "other". In most segmentation algorithms, the procedure returns the probability that a voxel belongs to a certain tissue class. This is generally called a fuzzy classification. For each voxel, we will assume that the probability for a tissue class approximates the underlying tissue composition. This implies that the segmentation probability is interpreted as a tissue fraction [11]. The set of segmentation images is then denoted $\{f^G, f^W, f^C, f^O\}$ and represents the a priori knowledge which will be incorporated in the reconstruction algorithm. Note that for each voxel j,

$$f_j^G + f_j^W + f_j^C + f_j^O = 1 \tag{1}$$

Differences in geometric alignment and image sampling grid are typical for images of the same patient using two different imaging modalities. Using a state-of-the-art image registration algorithm [17], it is possible to compute the affine transformation matrix $\mathcal{T}$ that is needed to align the MR image with the PET image. Of course, this action requires a preliminary reconstruction of the emission data. Since registration algorithms for the brain are very accurate, we will neglect registration errors. $\mathcal{T}$ is then also used to align the segmentation images of the MR data with the PET image.

B. Derivation of the algorithm

Due to a tracer activity distribution $\Lambda = \{\lambda_j \,|\, j = 1, \ldots, J\}$ in the field of view of a PET scanner, y_i photon pairs are measured at a line of response i. If λ_j represents the amount of activity at voxel j and c_{ij} is the probability that photons emitted in voxel j are detected in detector pair i, then $E(y_i) = \sum_j c_{ij}\lambda_j$ represents the expected amount of photon pairs. The matrix of detection probabilities $\{c_{ij}\}$ is called the system matrix and contains a mathematical description of the projection process with the associated physical effects that take place between emission and detection of photons. Since we assume that the measurements are samples from a Poisson distribution, the logarithm of the likelihood of measuring y_i, when $E(y_i)$ is expected, is

$$L = \sum_i \left[y_i \ln \left(\sum_j c_{ij}\lambda_j \right) - \sum_j c_{ij}\lambda_j - \ln(y_i!) \right] \tag{2}$$

If the logarithm of the prior M is used to impose additional constraints on the solution, we can compute the maximum-a-posteriori (MAP) estimator of Λ, given by

$$\Lambda = \arg\max_{\Lambda > 0} (L + M) \tag{3}$$

The system matrix, with elements c_{ij}, includes photon attenuation and position independent detector resolution (implemented as a convolution in sinogram space). We will ignore scatter and randoms in the theoretical framework of this paper.

Next, we define a number of subsets of the voxel space $\mathbb{J} = \{j \,|\, j = 1, \ldots, J\}$. These subsets are based on the anatomical information included in the segmentation images. The first set $\mathbb{B}$ corresponds to voxels belonging to the brain. The second set, complementary to $\mathbb{B}$, is denoted $\mathbb{O}$. These sets are defined by

$$\mathbb{B} = \{j \in \mathbb{J} \,|\, f_j^G + f_j^W + f_j^C > \epsilon_{\mathbb{B}}\} \tag{4}$$

$$\mathbb{O} = \mathbb{J} \setminus \mathbb{B} \tag{5}$$

with $0 < \epsilon_{\mathbb{B}} \ll 1$. Threshold parameter $\epsilon_{\mathbb{B}}$ controls the inclusion of voxels that are segmented into either GM, WM or CSF. This threshold value should be very small such that all voxels containing at least some fraction of one of the three tissue types are included. Set $\mathbb{B}$ is subdivided into two sets of voxels. These two sets are classified as voxels containing at least partially GM, denoted by $\mathbb{G}$, and the complementary part of $\mathbb{G}$ within $\mathbb{B}$, denoted by $\mathbb{N}$.

$$\mathbb{G} = \{j \in \mathbb{B} \,|\, f_j^G > \epsilon_{\mathbb{G}}\} \tag{6}$$

$$\mathbb{N} = \mathbb{B} \setminus \mathbb{G} \tag{7}$$

Threshold parameter $\epsilon_{\mathbb{G}}$ controls the inclusion of voxels with partially GM in $\mathbb{G}$. Since the GM tissue has our special attention in the further derivation of the algorithm, we include those voxels which contain at least some fraction of GM by

setting the threshold value very low, $0 < \epsilon_{\mathbb{G}} \ll 1$. Set $\mathbb{N}$ is subdivided into three subsets.

$$\mathbb{W} = \{j \in \mathbb{N} \,|\, f_j^W > (1-\epsilon_{\mathbb{W}})\} \quad (8)$$

$$\mathbb{C} = \{j \in \mathbb{N} \,|\, f_j^C > (1-\epsilon_{\mathbb{C}})\} \quad (9)$$

$$\mathbb{R} = \mathbb{N} \setminus (\mathbb{W} \cup \mathbb{C}) \quad (10)$$

For reasons that will become clear later, we want that voxels composed of mainly WM are included in subset $\mathbb{W}$ and voxels composed of mainly CSF are included in subset $\mathbb{C}$. Therefore, the threshold parameters should be very small, $0 < \epsilon_{\mathbb{W}} \ll 1$ and $0 < \epsilon_{\mathbb{C}} \ll 1$. The remaining voxels within $\mathbb{N}$, i.e. those voxels that contain a mixture of WM and CSF, are then included in subset $\mathbb{R}$.

Apart from these subsets, every PET voxel j can be thought of as a source with an activity λ_j equal to the total amount of fractional activities of the contributing tissues, or

$$\lambda_j = f_j^G \lambda_j^G + f_j^W \lambda_j^W + f_j^C \lambda_j^C + f_j^O \lambda_j^O \quad (11)$$

For $j \in \mathbb{G}$, we make an approximation of (11). Since both WM and CSF are expected to have an approximately uniform activity, we can replace the activity of these tissues in (11) with their mean activities calculated in regions $\mathbb{W}$ and $\mathbb{C}$ respectively. Furthermore, GM is surrounded by WM or CSF, which implies that $\forall j \in \mathbb{G} : f_j^O \approx 0$. Then, $\forall j \in \mathbb{G}$, equation (11) is approximated by

$$\lambda_j \approx f_j^G \lambda_j^G + f_j^W \bar{\lambda}^W + f_j^C \bar{\lambda}^C \quad (12)$$

with

$$\begin{aligned} \bar{\lambda}^W &= \frac{1}{n_{\mathbb{W}}} \sum_{l \in \mathbb{W}} f_l^W \lambda_l, & n_{\mathbb{W}} &= \sum_{l \in \mathbb{W}} f_l^W, \\ \bar{\lambda}^C &= \frac{1}{n_{\mathbb{C}}} \sum_{l \in \mathbb{C}} f_l^C \lambda_l, & n_{\mathbb{C}} &= \sum_{l \in \mathbb{C}} f_l^C. \end{aligned} \quad (13)$$

In (13), we assume that λ_l represents the "true" value for WM and CSF, respectively. This assumption can be made if $\epsilon_{\mathbb{W}}$ and $\epsilon_{\mathbb{C}}$ in (8) and (9) are very small. This implies that only voxels which are "almost" homogeneous in a certain tissue class are used. Then, instead of estimating $\Lambda = \{\lambda_j \,|\, j \in \mathbb{J}\}$, we estimate Λ^*, with

$$\Lambda^* = \{\lambda_j^* \,|\, j \in \mathbb{J}\} = \{\lambda_j^G \,|\, j \in \mathbb{G}\} \cup \{\lambda_j \,|\, j \in \mathbb{J} \setminus \mathbb{G}\} \quad (14)$$

This can be considered as a parameter transformation,

$$\begin{aligned} \forall j \in \mathbb{J} \setminus \mathbb{G} : \lambda_j &\longrightarrow \lambda_j = \lambda_j \\ \forall j \in \mathbb{G} : \lambda_j &\longrightarrow \lambda_j^G = \frac{\lambda_j - f_j^W \bar{\lambda}^W - f_j^C \bar{\lambda}^C}{f_j^G} \end{aligned} \quad (15)$$

This transformation allows us to estimate only the gray matter values, even in those voxels that contain a mixture of gray matter and other tissue classes. Then, by introducing the approximation made in equation (12) in $E(y_i) = \sum_j c_{ij} \lambda_j$, we can write that $E(y_i) \approx \sum_j c_{ij}^* \lambda_j^*$, for which

$$\begin{aligned} c_{ij}^* &= \delta_j^{\mathbb{G}} c_{ij} f_j^G + \delta_j^{\mathbb{W}} \frac{f_j^W}{n_{\mathbb{W}}} \left(\sum_{k \in \mathbb{G}} c_{ik} f_k^W \right) \\ &\quad + \delta_j^{\mathbb{C}} \frac{f_j^C}{n_{\mathbb{C}}} \left(\sum_{k \in \mathbb{G}} c_{ik} f_k^C \right) + \delta_j^{\mathbb{J} \setminus \mathbb{G}} c_{ij} \quad (16) \\ \lambda_j^* &= \delta_j^{\mathbb{G}} \lambda_j^G + \delta_j^{\mathbb{J} \setminus \mathbb{G}} \lambda_j \quad (17) \end{aligned}$$

with

$$\delta_l^{\mathbb{X}} \equiv \begin{cases} 1 & \Longleftrightarrow \quad l \in \mathbb{X} \\ 0 & \Longleftrightarrow \quad l \notin \mathbb{X} \end{cases} \quad (18)$$

This corresponds to a new system matrix c_{ij}^*. The derivation of c_{ij}^* is shown in Appendix II.

In $\mathbb{W}$, we impose a priori knowledge using a Gaussian prior, since $\mathbb{W}$ contains voxels composed of mainly WM which is expected to have an approximately uniform activity. This is done similarly for voxels within $\mathbb{C}$ and $\mathbb{R}$:

$$M^{\mathbb{W}} = -\frac{\beta_W}{2\sigma_W^2} \sum_{j \in \mathbb{W}} (\lambda_j - \bar{\lambda}^W)^2 \quad (19)$$

$$M^{\mathbb{C}} = -\frac{\beta_C}{2\sigma_C^2} \sum_{j \in \mathbb{C}} \lambda_j^2 \quad (20)$$

$$M^{\mathbb{R}} = -\frac{\beta_R}{2\sigma_R^2} \sum_{j \in \mathbb{R}} (\lambda_j - f_j^W \bar{\lambda}^W)^2 \quad (21)$$

with β_W, β_C, β_R the weights, σ_W, σ_C, σ_R the widths of the Gaussian priors, and $\bar{\lambda}^W$ defined in (13). The propagation of noise in $\mathbb{G}$ is controlled using a Gibbs smoothing prior, given by

$$M^{\mathbb{G}} = -\beta_g \sum_{j \in \mathbb{G}} \sum_{k \in \mathcal{N}_j^{\mathbb{G}}} \frac{1}{d_{jk}} \Phi(\lambda_j^G, \lambda_k^G) \quad (22)$$

with β_g the prior weight, d_{jk} the Euclidean distance between voxel j and k, $\mathcal{N}_j$ the neighborhood of voxel j with $j \notin \mathcal{N}_j$ and $\mathcal{N}_j^{\mathbb{G}} = \mathcal{N}_j \cap \mathbb{G}$, and Φ the local prior weight function based on a measure of the difference of activity between voxel j and voxel k. Then, the logarithm of the prior in (3) becomes

$$M = M^{\mathbb{W}} + M^{\mathbb{C}} + M^{\mathbb{R}} + M^{\mathbb{G}} \quad (23)$$

In Appendix I, we show that M is concave if $M^{\mathbb{G}}$ is concave. Moreover, since we assumed that the likelihood describes the Poisson nature of the emission data, the logarithm of the likelihood is concave under reasonable conditions [18]. Then, adding the concave logarithms of the likelihood and the prior gives a concave logarithm of the posterior. Consequently, the posterior has no multiple local maxima.

As in [19], we use a heuristic gradient ascent form of the expectation maximization (EM) approach for the optimization of (3). The iterative reconstruction algorithm is then given by

$$\lambda_j^{n+1} = \lambda_j^n + \lambda_j^n \frac{\left.\frac{\partial L}{\partial \lambda_j}\right|_{\vec{\lambda}^n} + \left.\frac{\partial M}{\partial \lambda_j}\right|_{\vec{\lambda}^n}}{\sum_i c_{ij} - \lambda_j^n \left.\frac{\partial^2 M}{\partial \lambda_j^2}\right|_{\vec{\lambda}^n}} \quad (24)$$

with n the iteration number and where we replace c_{ij} by c_{ij}^* and λ_j by λ_j^*. Finally, the reconstructed image is computed via the inverse transformation described in (15). This means that for all $j \in \mathbb{G}$, λ_j^G has to be replaced by

$$f_j^G \lambda_j^G + f_j^W \bar{\lambda}^W + f_j^C \bar{\lambda}^C \quad (25)$$

Henceforth, this iterative reconstruction algorithm is called Anatomical based MAP (A-MAP). The A-MAP algorithm is summarized in pseudo-code in Fig. 1.

A-MAP reconstruction algorithm

Initialization: $\lambda_j^* \leftarrow 1$

Precomputing c_{ij}^* using equation (16)

for n: $1 \rightarrow$ number of iterations **do**

$$\mathcal{P}_i \leftarrow \sum_j c_{ij}^* \lambda_j^* \qquad \text{(projection)}$$

$$\mathcal{B}_j \leftarrow \sum_i c_{ij}^* \left(\frac{y_i}{\mathcal{P}_i} - 1 \right) \qquad \text{(backprojection)}$$

$$\lambda_j^* \leftarrow \lambda_j^* + \lambda_j^* \frac{\mathcal{B}_j + \left. \frac{\partial M}{\partial \lambda_j} \right|_{\vec{\lambda}^*}}{\sum_i c_{ij}^* - \lambda_j^* \left. \frac{\partial^2 M}{\partial \lambda_j^2} \right|_{\vec{\lambda}^*}}$$

end

$$\lambda_j \leftarrow \delta_j^{\mathbb{J}\setminus\mathbb{G}} \lambda_j^* + \delta_j^{\mathbb{G}} \left(f_j^G \lambda_j^* + \frac{f_j^W}{n_{\mathbb{W}}} \sum_{l \in \mathbb{W}} f_l^W \lambda_l^* + \frac{f_j^C}{n_{\mathbb{C}}} \sum_{l \in \mathbb{C}} f_l^C \lambda_l^* \right)$$

Fig. 1. Pseudo-code of the anatomical based MAP reconstruction algorithm (A-MAP).

III. Experiments

We studied the performance of the proposed reconstruction algorithm for the detection of hypo-metabolic regions using two Monte-Carlo simulation experiments.

Because the shape of the human brain is complex, we constructed a clinically realistic brain phantom. This phantom was based on the three-dimensional (3D) digital phantom provided by the *BrainWeb* database [20]. To speed up simulations, experiments were performed on a two-dimensional (2D) trans-axial slice of the digital phantom with coordinates $z = 8$ mm in the stereo-tactical Talairach framework [21]. The digital phantom was used to make a baseline FDG-PET tracer distribution representing the glucose metabolism of a normal brain. We call this image the baseline phantom (BP). For that purpose, the GM, WM and CSF tissues were identified in the discrete anatomical model [22], called: the binary tissue maps of GM, WM and CSF. These tissue maps were smoothed using a two-dimensional isotropic Gaussian kernel with 2 mm full width at half maximum (FWHM) to simulate the output of (most) segmentation algorithms, i.e. fractional values which in our study are considered as tissue fractions. The baseline phantom was constructed by setting the activity to a clinically realistic number of 25 counts per voxel (cpv) in the GM region, 6.25 cpv in the WM region and 0 cpv in the CSF. Image dimensions are 217×217 voxels with an isotropic voxel size of 1 mm. In a duplicate of the baseline phantom, we selected five regions in the GM with a varying extent. The activity in these regions was decreased as in hypo-metabolic regions. We call this image the hypo-metabolic phantom (HP). The extent E in voxel units, the proportional decrease of activity Δ of the regions, as well as the long and short axis in voxel units of the ellipses that were used for the construction of the hypo-metabolic regions are listed in Table I.

The PET acquisition process was simulated by projection of the baseline and the hypo-metabolic phantom over 144 angles using a uniform attenuation image derived from the contour of the digital brain phantom and with a linear attenuation coefficient $\mu = 0.095\,\mathrm{cm}^{-1}$. To account for the finite resolution effect of the detector, both sinograms were smoothed along the detector grid using a one-dimensional (1D) Gaussian kernel with 5 mm FWHM. These sinograms were considered to be the noiseless PET measurements of the baseline and the hypo-metabolic phantoms. Of each sinogram a number of Poisson noise realizations were computed for use in the following two experiments.

In a first experiment, we studied the performance of the A-MAP algorithm in the detection of hypo-metabolic regions using the same anatomical information during reconstruction as for the construction of the phantoms. This is an ideal situation which enables us to study the optimal performance of using anatomical information.

In a second experiment, we studied the performance of the reconstruction algorithm for the detection of hypo-metabolic regions when using noisy and imperfect anatomical information during the reconstruction. For each noise realization of the emission data we constructed imperfect anatomical information. Because segmentation errors have a complex behavior, we approximated the concept of imperfect anatomical information by assuming that segmentation errors should occur at the tissue edges. We determined the inter-tissue interfaces of the binary tissue maps and within the two-voxel

TABLE I

The extent E in voxel units and the proportional decrease Δ of activity for the hypo-metabolic regions used in the design of the hypo-metabolic phantom. The last column shows the long and short axis in voxel units of the ellipses that were used for the construction of the hypo-metabolic regions. The GM activity was decreased within these ellipses.

Region number	E (voxels)	Δ (%)	Ellipse long – short axis (voxels)
1	43	20	12 – 6
2	28	22	10 – 5
3	42	24	12 – 5.3
4	44	20	15 – 6
5	45	20	9 – 9

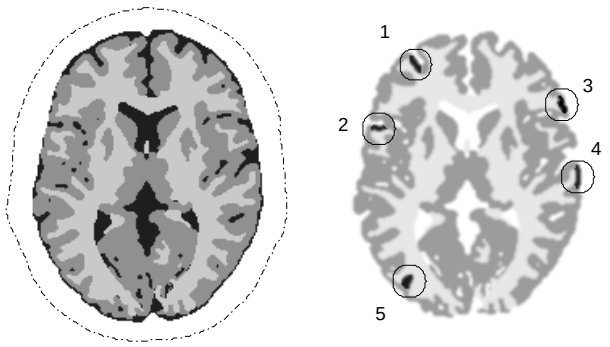

(a) (b)

Fig. 2. The composition of the binary tissue maps is shown in figure (a): CSF is indicated in black, GM in dark gray and WM in light gray. The outline of the uniform attenuation image is shown by the dash dot line. Within the outline the linear attenuation coefficient was set to $0.095\ \mathrm{cm}^{-1}$. The location of the hypo-metabolic regions is visualized in figure (b). The circles around each hypo-metabolic region i correspond to the regions-of-interest R_i.

thick edges we arbitrarily redistributed clustered parts of the anatomical information. Thereafter, the redistributed binary tissue maps were smoothed (as in experiment 1) using a two-dimensional isotropic Gaussian kernel with 2 mm FWHM to obtain fuzzy segmentations with the corresponding tissue fractions $\{f^G, f^W, f^C, f^O\}$. In the experiment, different anatomical labels with segmentation errors were generated. The probability of error was the same for all classes. It follows that the effect of these segmentation errors will be seen as an increase in variance, while it will have a negligible effect on the bias.

The following reconstruction parameter settings were used in both experiments: the threshold parameters are all set to a small value: $\epsilon_{\mathbb{G}} = 0.01$, $\epsilon_{\mathbb{B}} = 0.01$, $\epsilon_{\mathbb{W}} = 0.01$, $\epsilon_{\mathbb{C}} = 0.01$. In that way, $\mathbb{G}$ contains all voxels with at least 1 % GM, $\mathbb{W}$ contains voxels with more than 99 % WM, and $\mathbb{C}$ contains voxels with more than 99 % CSF. The global weight of the smoothing prior was $\beta_g = 8$. The global weights of the Gaussian priors and their widths were $\beta_W = \beta_C = \beta_R = 10$ and $\sigma_W = \sigma_C = \sigma_R = 3$, respectively. The choice for Φ in the Gibbs prior of equation (22) was based on the following rationale. Since the normal glucose metabolism in the GM of the human brain is not uniform but locally varying throughout the entire brain, the amount of penalty should not be based on the absolute, but rather on the relative difference of the activity of neighboring voxels. Moreover, the prior penalization term should become tolerant for differences that are large enough to be real. We have recently shown that these properties are elegantly combined in the relative difference (RD) prior [19], in which Φ is given by

$$\begin{aligned}\Phi(x_j, x_k) &= \frac{(x_j - x_k)^2}{x_j + x_k + \gamma|x_j - x_k|} \iff k \in \mathcal{N}_j \\ &= 0 \iff k \notin \mathcal{N}_j \end{aligned} \tag{26}$$

with $\mathcal{N}_j$ a neighborhood of j and γ a parameter controlling the point from which the prior becomes tolerant. Penalization is quadratic for small and linear for large differences. The factor $2/\gamma$ is related to an "intermediate" relative difference value. We assumed that a relative difference of 5 % was an intermediate value, such that γ was set to 40.

Next, in each experiment, the performance of the A-MAP algorithm was compared with post-smoothed maximum-likelihood expectation-maximization (ML-EM) and MAP-EM. We used the post-smoothed ML-EM reconstruction algorithm as the current golden standard in this evaluation process. ML-EM was implemented as described in (24) with $M = 0$ which is identical to the traditional implementation. The reconstructed image was post-smoothed using a two-dimensional isotropic Gaussian blurring kernel. The FWHM of this kernel was varied between 3 mm and 15 mm. We used the MAP-EM reconstruction algorithm as an indicator for the non-anatomical based use of prior information. The MAP-EM algorithm was implemented as described in (24) with

$$M = -\beta_g \sum_j \sum_{k \in \mathcal{N}_j} \frac{1}{d_{jk}} \Phi(\lambda_j, \lambda_k) \tag{27}$$

where Φ is given by (26) and $\mathcal{N}_j$ a 3×3 neighborhood. Ordered subsets [23] were used in all three algorithms. We used an iteration scheme with a decreasing number of subsets, consisting of (subsets $\times$ iterations): 36×5, 24×5, 18×5, 16×5, 12×5, 9×5, 8×5, 6×5, 4×5, 2×5, 1×10. This iteration scheme is almost equivalent to 685 regular iterations.

For notational convenience, we use the following symbols: B^{nl} and H^{nl} for the reconstructed images of the noiseless PET emission data of the baseline and the hypo-metabolic phantom, respectively; $\lambda_j(B^{(r)})$ and $\lambda_j(H^{(r)})$ for the values in voxel j of the reconstructed images of noise realization r of the PET emission data of the baseline and the hypo-metabolic phantom, respectively. B^{true} and H^{true} denotes the "true" baseline and hypo-metabolic phantom images, respectively.

The performance of each reconstruction algorithm was measured using a variety of metrics. First, the detection of hypo-metabolic regions was quantified using a computer observer [24]. In each experiment, for each reconstruction algorithm and for each noise realization r, we measured the response function

$$s_{\mathrm{nl}}(I^{(r)}, R) = \sum_{j \in R} (B_j^{\mathrm{nl}} - H_j^{\mathrm{nl}}) \cdot \lambda_j(I^{(r)}) \tag{28}$$

with I either B or H, and R a region of interest (ROI). The signal-to-noise ratio (SNR) for R was computed using

$$\mathrm{SNR}(R) = \sqrt{2 \frac{[\bar{s}(B) - \bar{s}(H)]^2}{\sigma_s^2(B) + \sigma_s^2(H)}} \tag{29}$$

with $\bar{s}(I)$ the mean and $\sigma_s^2(I)$ the variance of $s_{\mathrm{nl}}(I^{(r)}, R)$ over all noise realizations. Second, bias and variance measurements were performed. The bias image b was calculated using

$$b(I) = \bar{\lambda}(I) - I^{\mathrm{true}} \tag{30}$$

with $\bar{\lambda}(I)$ the mean of $\lambda(I^{(r)})$ over all noise realizations and I either B or H. The root mean squared (rms) bias $\tilde{b}(I, R)$ in ROI R was computed using

$$\tilde{b}(I, R) = \sqrt{\frac{1}{n_R} \sum_{j \in R} b_j^2(I)} \tag{31}$$

with n_R the number of voxels in R. The variance image $\sigma^2(I)$ was calculated using

$$\sigma^2(I) = \frac{1}{P-1} \sum_{r=1}^{P} \left(\lambda(I^{(r)}) - \bar{\lambda}(I) \right)^2 \tag{32}$$

with P the number of noise realizations. The rms standard deviation was computed using

$$\tilde{\sigma}(I, R) = \sqrt{\frac{1}{n_R} \sum_{j \in R} \sigma_j^2(I)} \tag{33}$$

IV. Results

The outline of the two-dimensional uniform attenuation image used in the reconstruction experiments is shown in Fig. 2(a). For visualization purposes, a composition of the binary tissue maps of GM, WM and CSF was constructed and is also shown in Fig. 2(a). In that image, CSF is indicated in black, GM in dark gray and WM in light gray. The baseline

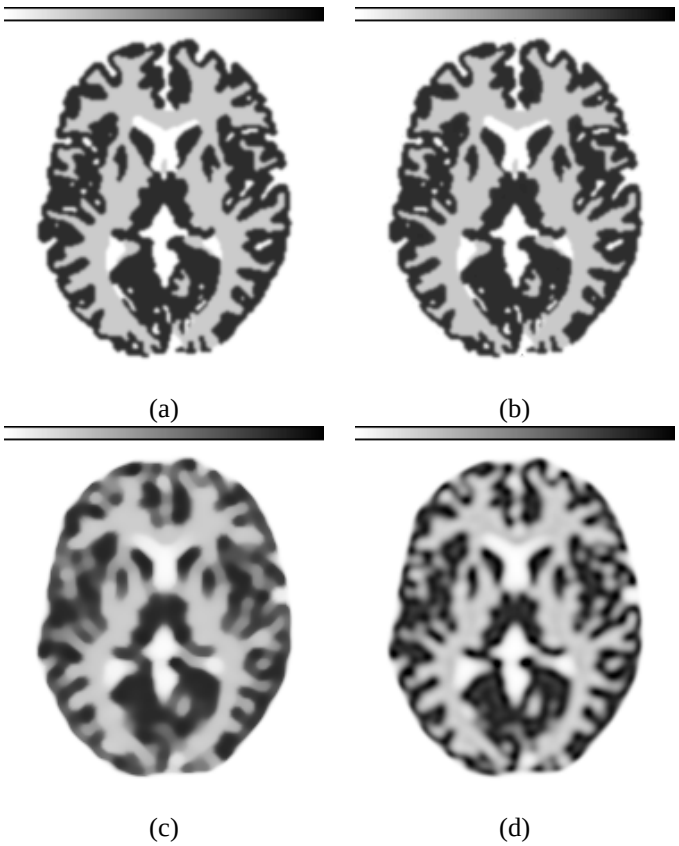

Fig. 3. The baseline "ground truth" phantom image is shown in (a). The remaining figures show the reconstructed images of the noiseless baseline phantom emission data. The A-MAP reconstruction, using $\beta_g = 8$, $\beta_W = \beta_C = \beta_R = 10$, and $\sigma_W = \sigma_C = \sigma_R = 3$, is shown in (b). The MAP-EM reconstruction, using $\beta_g = 8$, is shown in (c). The ML-EM reconstruction, without post-smoothing, is shown in (d). An iteration scheme with a decreasing number of subsets equivalent, to 685 regular iterations, was used. All images are scaled to the same intensity range. We used a color scale in which white corresponds to zero activity and black corresponds to an activity of 30 counts per voxel.

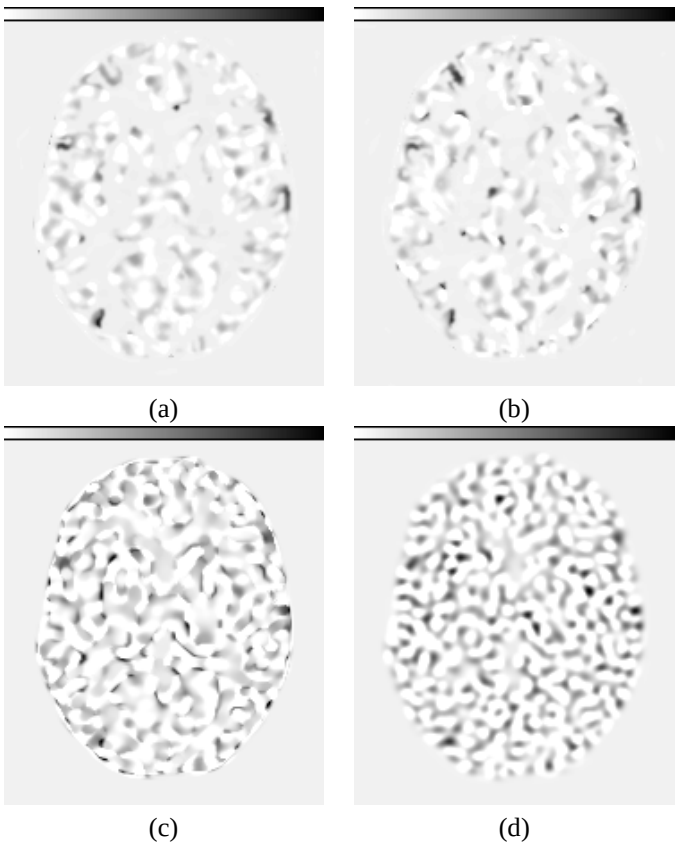

Fig. 4. The subtraction images of the reconstructions of a baseline and a hypo-metabolic noise realization, or $\lambda(B^{(r)}) - \lambda(H^{(r)})$, are shown for: (a) the A-MAP algorithm using perfect anatomical information (experiment 1), (b) the A-MAP algorithm using imperfect anatomical information (experiment 2), (c) the MAP-EM algorithm, and (d) the post-smoothed ML-EM algorithm using a two-dimensional isotropic Gaussian kernel with 4 mm FWHM. All images are scaled to the same intensity range, i.e. white corresponds to -0.5 cpv and black corresponds to 8 cpv.

phantom, constructed from the binary tissue maps, is shown in Fig. 3(a). This image acted as the baseline "ground truth" image. All experiments were performed using the software package IDL 5.1 (Research Systems, Inc.) on a Sun450 Model 4300 workstation (SUN Microsystems, Inc.).

A. Experiment 1

The A-MAP, using the exact anatomical information, the ML-EM and the MAP-EM reconstructed images of the noiseless PET emission data of the baseline are shown in Fig. 3(b–d). The noiseless projection data of the baseline phantom contained 8.6 Mcounts. For this experiment, we computed $P = 700$ Poisson noise realizations of the noiseless PET emission data of the baseline and the hypo-metabolic phantom. The subtraction images of the reconstructions of a baseline and a hypo-metabolic noise realization are shown in Fig. 4(a, c, and d). The SNR results for each reconstruction algorithm and for different regions-of-interest are shown in Table II. The SNR values were scaled with respect to the SNR of the MAP-EM algorithm for comparison. The bias images $b(B)$ are displayed in Fig. 5(a, c, and d). For reasons of dynamic range, variance images were converted to standard deviation images and are displayed in Fig. 6(a, c, and d). The rms bias and rms standard deviation results in different ROIs in the reconstructions of the hypo-metabolic phantom data are shown in Fig. 7. For all reconstruction algorithms, a ROI equal to all voxels in the brain was used. The rms bias and rms standard deviation was also calculated within circular ROIs around each hypo-metabolic region, as shown in Fig. 2(b). Finally, line profiles were computed through hypo-metabolic region number 1 of the mean reconstructed images $\bar{\lambda}(B)$ and $\bar{\lambda}(H)$. The difference between these line profiles for each algorithm are shown in Fig. 8.

B. Experiment 2

For this experiment, we computed $P = 400$ Poisson noise realizations of the noiseless PET emission data of the baseline and the hypo-metabolic phantom. Four hundred different imperfect anatomical label maps were computed. Using these maps, the A-MAP reconstruction of the noisy emission data of the baseline and the hypo-metabolic phantom was performed and the figures of merit were calculated. The SNR results for each reconstruction algorithm and for different regions-of-interest are shown in Table II. Again, the SNR values were scaled with respect to the SNR of the MAP-EM algorithm, for

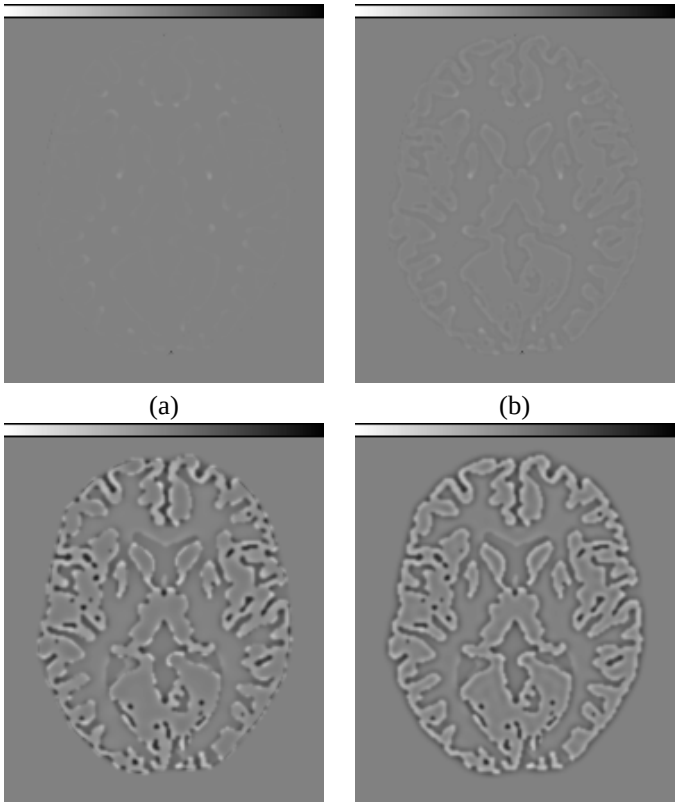

Fig. 5. The bias images $b(B)$ of the reconstruction experiments, when using: (a) the A-MAP algorithm using perfect anatomical information (experiment 1), (b) the A-MAP algorithm using imperfect anatomical information (experiment 2), (c) the MAP-EM algorithm, and (d) the post-smoothed ML-EM algorithm using a two-dimensional isotropic Gaussian kernel with 4 mm FWHM. All images are the result from simulations where Poisson noise was used, except in the case of (b), where simulations included both Poisson noise and noise from MRI segmentations. All images are scaled to the same intensity range, i.e. white corresponds to -20 counts per voxel (cpv) and black corresponds to $+20$ cpv.

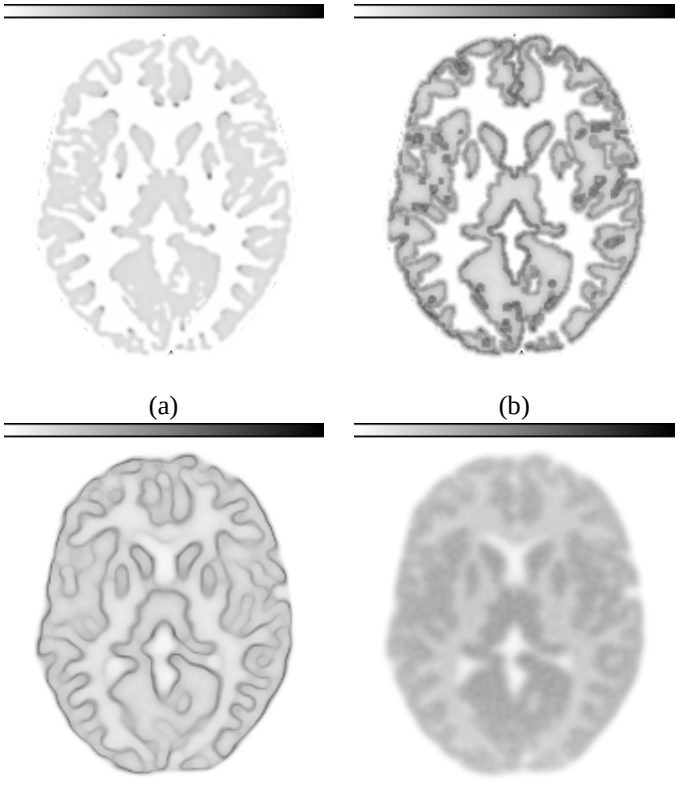

Fig. 6. The standard deviation images $\sigma(B)$ of the reconstruction experiments, when using: (a) the A-MAP algorithm with perfect anatomical information (experiment 1), (b) the A-MAP algorithm with noisy and imperfect anatomical information (experiment 2), (c) the MAP-EM algorithm in experiment 1, and (d) the post-smoothed ML-EM algorithm using a two-dimensional isotropic Gaussian kernel with 4 mm FWHM (experiment 1). All images are the result from simulations where Poisson noise was used, except in the case of (b), where simulations included both Poisson noise and noise from MRI segmentations. All images are scaled to the same intensity range, i.e. white corresponds to zero and black corresponds to 5 cpv.

comparison. The subtraction image of the reconstruction of a baseline and a hypo-metabolic noise realization are shown in Fig. 4(b). The bias image $b(B)$ of the A-MAP algorithm is shown in Fig. 5(b). The standard deviation image of A-MAP is shown in Fig. 6(b). The root mean squared (rms) bias and rms standard deviation results in different ROIs in the A-MAP reconstruction of the hypo-metabolic phantom data are shown in Fig. 7.

V. Discussion

The aim of this study is the design of an iterative reconstruction algorithm, dedicated for the detection of hypo-metabolic regions in FDG-PET brain images of epilepsy patients. In view of an improved detection capability, prior knowledge is included in the reconstruction process. This prior knowledge is partly based on information derived from MR data and partly based on information about the underlying pathology. No anatomical information about the presence, location or extent of possible candidate epileptogenic regions is used during the reconstruction process. This approach is often called to be a case of "missing labels". Using the anatomical information, we established a correction scheme for the partial volume effect. The resolution recovery, on the other hand, will account for the spill over effect during the reconstruction process. It is clear that a reconstruction algorithm that aims for a sufficient partial volume correction, should at least include a projection model that accounts for the resolution effect. Equations (16) and (17) show how the parameter transformation is reflected in an adjusted projection and back-projection operator. The correction for the partial volume effect of WM and CSF in the GM region is shown in the second and third term of the new system matrix (16). The finite resolution and the attenuation are included in the definition of the original system matrix, i.e. without the anatomical information. The additional use of priors is used to suppress the propagation of noise.

With the A-MAP reconstruction algorithm, we have included anatomical information during the reconstruction process as opposed to post-processing methods. Recently, we have compared the noise characteristics (SNR) of the A-MAP method with that of post-processed ML-EM for the incorporation of anatomical information, and with post-smoothed ML-EM without the use of anatomical information [27]. The "straightforward" post-processing of the ML-EM reconstruction shows inferior performance compared to both A-MAP

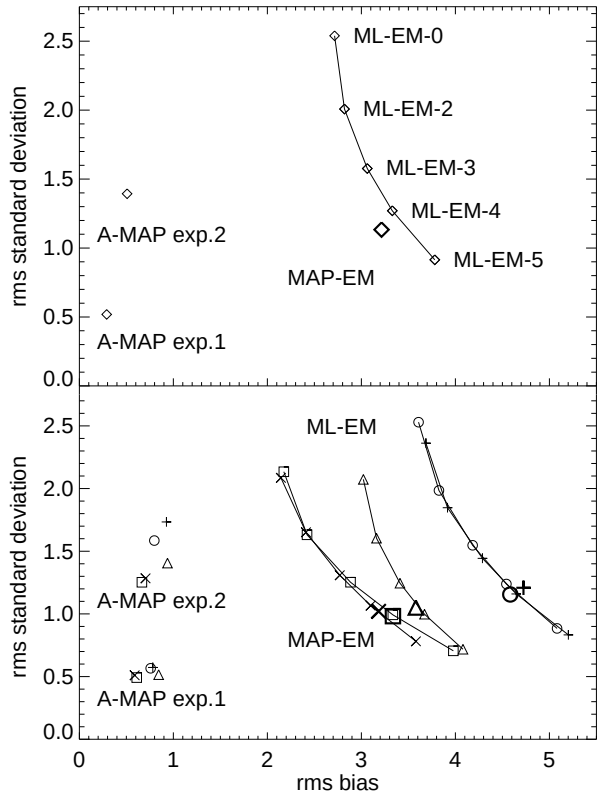

Fig. 7. In these diagrams the root mean squared (rms) bias $\tilde{b}$ and the rms standard deviation $\tilde{\sigma}$ are shown for the reconstructions based on the hypo-metabolic phantom data. In the upper plot, the diamond shaped data points ($\diamond$) show the results for a ROI equal to all voxels in the brain. In the lower plot, the rms bias and rms standard deviation are also shown for circular ROIs around hypo-metabolic region 1 ($+$), 2 ($\bigcirc$), 3 ($\triangle$), 4 ($\square$), and 5 ($\times$). Only the results of experiment 1 are displayed for the MAP-EM and ML-EM algorithms. Poisson noise was used in all simulations, except in the case of A-MAP exp. 2, where simulations included both Poisson noise and noise from MRI segmentations. ML-EM-X means post-smoothed ML-EM using a two-dimensional isotropic Gaussian kernel with X mm FWHM. For the MAP-EM algorithm, the symbols are thicker and a little larger. For the ML-EM algorithm, the symbols belonging to the same ROI are connected by a solid line.

TABLE II

RESULTS OF THE SIGNAL-TO-NOISE RATIO (SNR) FOR BOTH EXPERIMENTS AND FOR DIFFERENT REGIONS-OF-INTEREST (ROI): $\mathbb{J}$, THE WHOLE IMAGE, AND R_i A CIRCULAR ROI, WITH A TEN VOXEL WIDE RADIUS, CENTERED AT THE LOCATION OF THE HYPO-METABOLIC REGION i. THE SNR RESULTS OF A-MAP AND ML-EM WERE RELATIVELY SCALED WITH RESPECT TO THE MAP-EM ALGORITHM. ML-EM-X MEANS POST-SMOOTHED ML-EM USING A TWO-DIMENSIONAL ISOTROPIC GAUSSIAN KERNEL WITH X MM FWHM.

Experiment 1, $P = 700$ noise realizations						
Algorithm	SNR					
	$\mathbb{J}$	R_1	R_2	R_3	R_4	R_5
A-MAP	1.24	1.26	1.17	1.29	1.22	1.31
MAP-EM	1.00	1.00	1.00	1.00	1.00	1.00
ML-EM-0	0.77	0.74	0.76	0.80	0.74	0.77
ML-EM-4	1.01	0.97	0.98	1.06	1.05	1.02
ML-EM-8	1.25	1.26	1.22	1.23	1.20	1.30
ML-EM-12	1.24	1.28	1.18	1.25	1.18	1.30
ML-EM-15	1.20	1.27	1.13	1.23	1.17	1.27
Experiment 2, $P = 400$ noise realizations						
Algorithm	SNR					
	$\mathbb{J}$	R_1	R_2	R_3	R_4	R_5
A-MAP	0.98	0.86	0.86	1.15	0.98	1.09
MAP-EM	1.00	1.00	1.00	1.00	1.00	1.00
ML-EM-0	0.77	0.75	0.76	0.79	0.75	0.79
ML-EM-4	1.01	0.97	0.99	1.05	1.05	1.02
ML-EM-8	1.23	1.25	1.22	1.22	1.22	1.24
ML-EM-12	1.23	1.28	1.16	1.23	1.20	1.24
ML-EM-15	1.20	1.27	1.11	1.22	1.18	1.23

and post-smoothed ML-EM. However, if a prewhitening step is added to the post-processing method, results are comparable to both A-MAP and post-smoothed ML-EM. Unfortunately, the prewhitening procedure involves the application of a shift variant filter which makes the implementation more complicated than that of A-MAP.

In the derivation of the reconstruction method, we use the concept of a tissue composition model, as proposed by [11]. In that paper, that concept was used in combination with two regularization functions. The first function, a Gaussian prior, was used to impose a Gaussian distribution to the fractional activity of each tissue. The second function, a Gibbs prior, was used to smooth the fractional activities of identical neighboring tissues. In our method, we use a Gaussian prior to meet the approximately uniform activity assumptions for the WM and CSF. For the GM tissue, that type of regularization can not be used, because normal GM glucose metabolism is locally varying throughout the brain. Moreover, the purpose of this method is to improve the detection of regions with a decreased GM metabolism. Because tracer uptake in GM is not expected to be uniform, we do not wish to use a Gaussian intensity distribution as a prior, as was done for WM and CSF. Instead, we apply a Gibbs prior that tends to preserve strong edges. Because of partial volume effects, straightforward application of this prior would result in smoothing over the boundaries between GM and WM. This was avoided by using (12) and (15): in voxels that contain a mixture of WM and GM, the effect of the prior is restricted to the GM contribution.

In clinical practice, occasionally extra-nasal activity can be seen in FDG-PET scans. We can reasonably assume that the activity will be enclosed in the subset $\mathbb{O}$. There, A-MAP reconstructs this activity distribution as in MAP-EM.

Note that the iterative optimization structure, of the MAP based reconstruction algorithm (24), was not altered in the derivation of our algorithm. In fact, one could easily use other optimization schemes. The major change in A-MAP was made by the use of a parameter transformation.

We assume that, using the proposed reconstruction algorithm, the physician will be able to differentiate more easily between real hypo-metabolic regions and regions with a decreased intensity due to the partial volume effect. For that reason, we expect an improvement in the detection of subtle hypo-metabolic regions, whereas larger regions should already be visible using the current existing reconstruction techniques.

It is clear that the detection performance of A-MAP depends on the accuracy of the anatomical information. However, we feel that current MR acquisition sequences perform very well and image quality gives a good contrast-to-noise ratio for the

brain tissues. By that, current state-of-the-art segmentation algorithms can perform to the best of their ability. Although it was not the purpose of this study to investigate the optimal choice for the threshold parameters ϵ, we found that the chosen values gave good results when performing some preliminary testing. Further research should involve a more profound analysis of the performance of A-MAP under more realistic circumstances.

Experiment 1 compared the performance of post-smoothed ML-EM and regular MAP-EM with that of A-MAP using perfect anatomical information. For ML-EM a bias-noise curve was generated by varying the width of the post-smoothing kernel (Fig. 7). The MAP-EM result is very close to the ML-EM curve. This seems in agreement with [25], [26], who observed very similar noise characteristics for MAP-EM (or penalized likelihood) and post-smoothed ML-EM at matched resolution. These results also show that the post-smoothed ML-EM images using 4 mm FWHM have a good bias-noise trade-off. For that reason, we show the results of ML-EM using 4 mm FWHM for comparison with A-MAP in Fig. 4, Fig. 5, and Fig. 6. The result of A-MAP yields a point at the left of this curve, implying that A-MAP produces lower bias at matched noise levels. By varying the parameters of the prior, a bias-noise curve could be produced for A-MAP as well. The optimal point along that curve will depend on the application, and may well be very different for such tasks as visual inspection and quantitative analysis.

Table II reports the SNR results for lesion detection by the non-prewhitening numerical observer. A-MAP yielded SNR values close to the best values obtained with post-smoothed ML-EM. This is in agreement with [27], where we found no significant difference between the optimal SNR of A-MAP and the optimal SNR of post-smoothed ML-EM for simulation experiments using a simplified Shepp-Logan phantom.

With the second experiment, we illustrate the performance of A-MAP in a more challenging situation, i.e. using imperfect anatomical information. In general, a whole variety of effects can contribute to the concept of imperfect anatomical information, e.g. registration errors, segmentation errors, randoms, scatter, patient movement during the measurement. Since the joint behavior of all of these effects concerning the introduction of errors is probably very complex, we focus to segmentation errors for this study. That is, we assumed that errors introduced by poor segmentation of the MR image lead to imperfect anatomical information.

The results of experiment 2 show an overall slight reduction of the SNR for A-MAP, compared to MAP-EM. Only hypo-metabolic regions 3 and 5 give better SNR results when using A-MAP. The rms bias of A-MAP is lower than MAP-EM and post-smoothed ML-EM. The more pronounced increase of the rms standard deviation compared to the rms bias between the first and the second experiment for the A-MAP algorithm, as can be seen in Fig. 7, was in fact expected due to the specific design of the second experiment. In that experiment, four hundred different imperfect anatomical label maps were used. As a result, the effect of anatomical errors shows up in our analysis as an increase in variance (Fig. 6). Because these errors are random in all directions with the same probabilities,

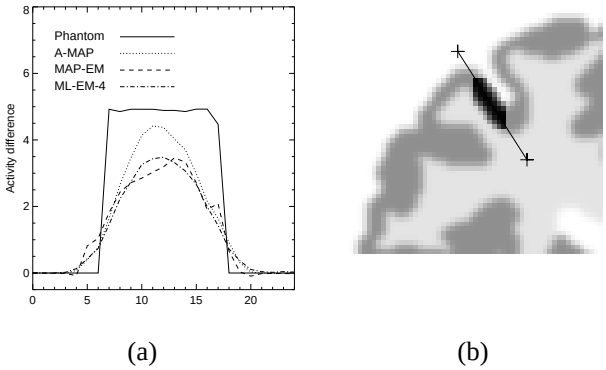

(a) (b)

Fig. 8. Plot (a) shows the activity profile of $\bar{\lambda}_j(B) - \bar{\lambda}_j(H)$ through hypo-metabolic region number 1 for A-MAP, MAP-EM and post-smoothed ML-EM using a two-dimensional isotropic Gaussian kernel with 4 mm FWHM (experiment 1). Figure (b) shows the exact location of the line profile in an enlargement of the upper-left corner of the image that shows the location of the hypo-metabolic regions.

there is no effect on the bias (as confirmed by Fig. 5). Note that in clinical applications possible segmentation errors may lead to an increase of bias. The slight reduction of the SNR results of A-MAP compared to MAP-EM in the second experiment can be attributed to the template based approach of the SNR computation. The size of the hypo-metabolic regions in the reconstructed image will vary together with the variation in the anatomical information. Inevitably, this influences the value of the signal response, as computed using (28).

VI. Conclusion

We can conclude that the use of anatomical information combined with prior information about the underlying pathology is very promising for the detection of subtle hypo-metabolic regions in the brain of epilepsy patients. Further evaluation of the algorithm, using realistic data, is underway.

Acknowledgment

The authors wish to thank Dirk Vandermeulen, Siddharth Srivastava and Dirk Bequé for useful discussions regarding this study, as well as the anonymous referees for their constructive comments.

Appendix I

We prove that the logarithm of the prior M, defined in equations (19-23), is concave, if $M^{\mathbb{G}}$ is concave.

Proof: It has to be shown that the matrix of second derivatives of the logarithm of the prior is negative semi-definite, or

$$\sum_{k,l} x_k x_l \frac{\partial^2 M}{\partial \lambda_k \partial \lambda_l}\bigg|_{\vec{x}} \leq 0 \tag{34}$$

for all $\vec{x} = \{x_j \mid j \in \mathbb{J}\}$. Since the sum of concave functions is concave, and given $M^{\mathbb{G}}$ is concave, it is sufficient to prove that $M^{\mathbb{W}}$, $M^{\mathbb{C}}$ and $M^{\mathbb{R}}$ are concave. It is clear that $M^{\mathbb{C}}$ is concave. Then, for this proof it remains to be shown that $M^{\mathbb{W}}$ and $M^{\mathbb{R}}$ are concave. We proof this for $M^{\mathbb{W}}$ and without loss of generality, we assume that $\beta_W = \sigma_W = 1$. Then, for

all $k, l \in \mathbb{W}$, the matrix of second derivatives contains the following elements:

$$\frac{\partial^2 M^{\mathbb{W}}}{\partial \lambda_k^2} = -1 + 2\frac{f_k}{n_{\mathbb{W}}} - N\frac{f_k^2}{n_{\mathbb{W}}^2} \quad (35)$$

$$\frac{\partial^2 M^{\mathbb{W}}}{\partial \lambda_k \partial \lambda_l} = \frac{1}{n_{\mathbb{W}}}\left(f_k + f_l - N\frac{f_k f_l}{n_{\mathbb{W}}}\right) \quad (36)$$

with $N = \sum_{j\in\mathbb{W}}$ and $n_{\mathbb{W}}$ defined in (13). For $M = M^{\mathbb{W}}$, equation (34) becomes

$$\frac{2}{n_{\mathbb{W}}}\left(\sum_{k\in\mathbb{W}} x_k\right)\left(\sum_{k\in\mathbb{W}} x_k f_k\right) \stackrel{?}{\leq} \sum_{k\in\mathbb{W}} x_k^2 + \frac{N}{n_{\mathbb{W}}^2}\left(\sum_{k\in\mathbb{W}} x_k f_k\right)^2 \quad (37)$$

Using

$$\left(\frac{1}{\sqrt{N}}\sum_{k\in\mathbb{W}} x_k - \frac{\sqrt{N}}{n_{\mathbb{W}}}\sum_{k\in\mathbb{W}} x_k f_k\right)^2 \geq 0 \quad (38)$$

we can construct the following inequality:

$$\frac{2}{n_{\mathbb{W}}}\left(\sum_{k\in\mathbb{W}} x_k\right)\left(\sum_{k\in\mathbb{W}} x_k f_k\right) \leq \frac{1}{N}\left(\sum_{k\in\mathbb{W}} x_k\right)^2 + \frac{N}{n_{\mathbb{W}}^2}\left(\sum_{k\in\mathbb{W}} x_k f_k\right)^2 \quad (39)$$

With the use of Cauchy-Schwartz inequality, it is easy to prove equation (37). The proof for the concavity of $M = M^{\mathbb{R}}$ is similar. Hence, M is concave. ■

APPENDIX II

System matrix c_{ij}^*, as shown in (16), is derived by introducing (12) in $E(y_i) = \sum_j c_{ij}\lambda_j$,

$$E(y_i) \approx \sum_{j\in\mathbb{G}} c_{ij}\left(f_j^G\lambda_j^G + \frac{f_j^W}{n_{\mathbb{W}}}\sum_{l\in\mathbb{W}} f_l^W\lambda_l + \frac{f_j^C}{n_{\mathbb{C}}}\sum_{l\in\mathbb{C}} f_l^C\lambda_l\right) + \sum_{j\in\mathbb{J}\setminus\mathbb{G}} c_{ij}\lambda_j \quad (40)$$

$$= \sum_{j\in\mathbb{G}} c_{ij}f_j^G\lambda_j^G + \sum_{j\in\mathbb{J}\setminus\mathbb{G}}\left[\delta_j^{\mathbb{W}}\frac{f_j^W}{n_{\mathbb{W}}}\left(\sum_{k\in\mathbb{G}} c_{ik}f_k^W\right)\lambda_j + \delta_j^{\mathbb{C}}\frac{f_j^C}{n_{\mathbb{C}}}\left(\sum_{k\in\mathbb{G}} c_{ik}f_k^C\right)\lambda_j + c_{ij}\lambda_j\right] \quad (41)$$

$$= \sum_j c_{ij}^*\lambda_j^* \quad (42)$$

with c_{ij}^* defined in (16), λ_j^* defined in (17), and $\delta_j^{\mathbb{X}}$ defined in (18).

REFERENCES

[1] G.L. Westbrook, "Seizures and epilepsy" in *Principles of neural science*, 4th ed., E.R. Kandel, J.H. Schwartz, and T.M. Jessell, Eds. New York, NY: McGraw-Hill, 2000, pp. 910–935.

[2] F. Rosenow and H. Lüders, "Presurgical evaluation of epilepsy," *Brain*, vol. 124, no. 9, pp. 1683–1700, Sep. 2001.

[3] S. Asenbaum and C. Baumgartner, "Nuclear medicine in the preoperative evaluation of epilepsy," *Nucl. Med. Commun.*, vol. 21, pp. 835–840, Jul. 2001.

[4] W.H. Theodore, S. Sato, C.V. Kufta, W.D. Gaillard, and K. Kelley, "FDG-positron emission tomography and invasive EEG: seizure focus detection and surgical outcome," *Epilepsia*, vol. 38, no. 1, pp. 81–86, Jan. 1997.

[5] B. Fischl and A.M. Dale, "Measuring the thickness of the human cerebral cortex from magnetic resonance images," *Proc. Natl. Acad. Sci. USA*, 2000, vol. 97, no. 20, pp. 11050–11055.

[6] F. Fazio and D. Perani, "Importance of partial-volume correction in brain PET studies," *J. Nucl. Med.*, vol. 41, no. 11, pp. 1849–1850, Nov. 2000.

[7] H.W. Müller-Gärtner, J.M. Links, J.L. Prince, R.N. Bryan, E. McVeigh, J.P. Leal, C. Davatzikos, and J.J. Frost, "Measurement of radiotracer concentration in brain gray matter using positron emission tomography: MRI-based correction for partial volume effects," *J. Cereb. Blood Flow Metab.*, vol. 12, no. 4, pp. 571–583, 1992.

[8] C. Comtat, P.E. Kinahan, J.A. Fessler, T. Beyer, D.W. Townsend, M. Defrise, and C. Michel, "Clinically feasible reconstruction of 3D whole-body PET/CT data using blurred anatomical labels," *Phys. Med. Bio.*, vol. 47, pp. 1–20, Jun. 2002.

[9] J.A. Fessler, N.H. Clinthorne, and W.L. Rogers, "Regularized emission image reconstruction using imperfect side information," *IEEE Trans. Nucl. Sc.*, vol. 39, no. 5, pp. 1464–1471, Oct. 1992.

[10] B. Lipinski, H. Herzog, E. Rota Kops, W. Oberschelp, and H.W. Müller-Gärtner, "Expectation maximization reconstruction of positron emission tomography images using anatomical magnetic resonance information," *IEEE Trans. Med. Imag.*, vol. 16, no. 2, pp. 129–136, Apr. 1997.

[11] S. Sastry, and R.E. Carson, "Multimodality Bayesian algorithm for image reconstruction in positron emission tomography: a tissue composition model," *IEEE Trans. Med. Imag.*, vol. 16, no. 6, pp. 750–761, Dec. 1997.

[12] B.A. Ardekani, M. Braun, B.F. Hutton, I. Kanno, and H. Iida, "Minimum cross-entropy reconstruction of PET images using prior anatomical information," *Phys. Med. Bio.*, vol. 41, pp. 2497–2517, Jun. 1996.

[13] A. Rangarajan, I.-T. Hsiao, and G. Gindi, "A bayesian joint mixture framework for the integration of anatomical information in functional image reconstruction," *J. Math. Imag. Vision*, vol. 12, no. 3, pp. 119–217, Jun. 2000.

[14] S.C. Huang, M.E. Phelps, E.J. Hoffman, K. Sideris, C.J. Selin, and D.E. Kuhl, "Noninvasive determination of local cerebral metabolic rate of glucose in man," *Am. J. Physiol.*, vol. 238, pp. E69–E82, 1980.

[15] F. Turkheimer, R.M. Moresco, G. Lucignani, L. Sokoloff, F. Fazio, and K. Schmidt, "The use of spectral analysis to determine regional cerebral glucose utilization with positron emission tomography and [^{18}F]fluorodeoxyglucose: theory, implementation, and optimization procedures," *J. Cereb. Blood Flow Metab.*, vol. 14, no. 3, pp. 406–422, 1994.

[16] K. Van Leemput, F. Maes, D. Vandermeulen, and P. Suetens, " Automated model-based tissue classification of MR images of the brain," *IEEE Trans. Med. Imag.*, vol. 18, no. 10, pp. 897–908, Oct. 1999.

[17] F. Maes, A. Collignon, D. Vandermeulen, G. Marchal and P. Suetens, "Multimodality image registration by maximization of mutual information," *IEEE Trans. Med. Imag.*, 1997, vol.16, no. 2, pp. 187–198.

[18] L.A. Shepp and Y. Vardi, "Maximum likelihood reconstruction for emission tomography," *IEEE Trans. Med. Imag.*, vol. 1, no. 2, pp. 113–122, 1982.

[19] J. Nuyts, D. Bequé, P. Dupont and L. Mortelmans, "A concave prior penalizing relative differences for maximum-a-posteriori reconstruction in emission tomography," *IEEE Trans. Nucl. Sc.*, vol. 49, no. 1, pp. 56–60, Feb. 2002.

[20] (2002) BrainWeb. [Online]. Available: http://www.bic.mni.mcgill.ca/brainweb/

[21] J. Talairach and P. Tournoux, "Co-planar stereotaxic atlas of the human brain," Thieme, New York, 1988.

[22] D.L. Collins, A.P. Zijdenbos, V. Kollokian, J.G. Sled, N.J. Kabani, C.J. Holmes, and A.C. Evans, "Design and construction of a realistic digital brain phantom," *IEEE Trans. Med. Imag.*, vol. 17, no. 3, pp. 463–468, Jun. 1998.

[23] H.M. Hudson and R.S. Larkin, "Accelerated image reconstruction using ordered subsets of projection data," *IEEE Trans. Med. Imag.*, vol. 13, no. 4, pp. 601–609, Dec. 1994.

[24] R.F. Wagner and D.G. Brown, "Unified SNR analysis of medical imaging systems," *Phys. Med. Bio.*, vol. 30, no. 6, pp. 489–518, Jun. 1985.

[25] J. Nuyts and J.A. Fessler, "A penalized-likelihood image reconstruction method for emission tomography, compared to post-smoothed maximum-likelihood with matched spatial resolution," *IEEE Trans. Med. Imag.*, vol. 22, no. 9, pp. 1042–1052, Sep. 2003.

[26] J.W. Stayman, and J.A. Fessler, "Compensation for nonuniform resolution using penalized-likelihood reconstruction in space-variant imaging systems," *IEEE Trans. Med. Imag.*, in press, 2003.

[27] J. Nuyts, K. Baete, D. Bequé, and P. Dupont, "Comparison between MAP and post-processed ML for incorporating anatomical knowledge in emission tomography," *Proc. IEEE Nuc. Sci. Symp. and Med. Imag. Conf.*, M5-2, Portland, Oregon, USA, Oct. 2003.